

Mid-infrared optical coherence tomography

Christopher S. Colley, Jeremy C. Hebden, and David T. Delpy

Department of Medical Physics and Bioengineering, University College London, Malet Place Engineering Building, Gower Street, London WC1E 6BT, United Kingdom

Alison D. Cambrey and Robert A. Brown

Institute of Orthopaedics & Musculoskeletal Science, University College London, Brockley Hill, Stanmore, Middlesex HA7 4LP, United Kingdom

Evgeny A. Zibik, Wing H. Ng, Luke R. Wilson, and John W. Cockburn

Department of Physics and Astronomy, University of Sheffield, Sheffield S3 7RH, United Kingdom

(Received 22 October 2007; accepted 15 November 2007; published online 18 December 2007)

A time domain optical coherence tomography (OCT) system is described that uses mid-infrared light (6–8 μm). To the best of our knowledge, this is the first OCT system that operates in the mid-infrared spectral region. It has been designed to characterize bioengineered tissues in terms of their structure and biochemical composition. The system is based upon a free-space Michelson interferometer with a germanium beam splitter and a liquid nitrogen cooled HgCdTe detector. A key component of this work has been the development of a broadband quantum cascade laser source (InGaAs/AlInAs containing 11 different active regions of the three well vertical transition type) that emits continuously over the 6–8 μm wavelength range. This wavelength range corresponds to the so called “mid-infrared fingerprint region” which exhibits well-defined absorption bands that are specifically attributable to the absorbing molecules. Therefore, this technology provides an opportunity for optical coherence molecular imaging without the need for molecular contrast agents. Preliminary measurements are presented. © 2007 American Institute of Physics.

[DOI: [10.1063/1.2821609](https://doi.org/10.1063/1.2821609)]

I. INTRODUCTION

Since its introduction in the early 1990s, optical coherence tomography (OCT) at visible and near-infrared (NIR) wavelengths has emerged as a powerful technique for noninvasive cross-sectional imaging of turbid media, such as biological tissues. OCT is a straight ray tomographic method, analogous to diagnostic ultrasound, whereby depth positions of reflecting boundaries within a sample are measured using coherent interference between a probe beam and a reference derived from the same source. Axial resolution is decoupled from transverse resolution and is determined by the coherence length and, therefore, the bandwidth of the light source. The focus of much OCT development has been on medical applications since the first (*in vitro*) OCT images were presented in 1991, using a low coherence interferometer.¹ Detailed aspects of OCT theory and applications have been reviewed previously.^{2–5}

Researchers in regenerative medicine have identified an urgent need for real-time sensors to provide a noninvasive assessment of the structure and biochemical content of engineered tissues during the growth cycle. Consequently, there is interest in the application of OCT to tissue engineering.^{6–9} New monitoring techniques are essential in order to guide the remodeling processes in bioreactors, the mechanisms of which remain largely unknown. There is also a great need for minimally invasive monitoring of postimplantation tissues, particularly for orthopaedic engineered implants, since clinical failure can take months or years, making research, regulation, and clinical assessment slow and expensive.

While materials such as bone and collagen absorb rela-

tively little within the range of visible and near-infrared wavelengths used in existing OCT systems, the mid-infrared (MIR) region is dominated by absorption bands specifically attributable to compounds such as collagen amide, phosphate, and carbonate. The characteristic MIR absorption by these biochemical species therefore provides a potentially powerful method of imaging tissue constructs growing in bioreactors and implanted *in vivo*.

So far, the MIR region of the electromagnetic spectrum has not yet been widely exploited for imaging due to a lack of appropriate sources and other essential passive components. However, the recent emergence of quantum cascade laser (QCL) technology for MIR sources promises to make feasible new diagnostic techniques with a potentially broad range of uses in both the medical and industrial fields. In this article, a MIR-OCT system is described which, to the best of our knowledge, is the first such system. It will be used to noninvasively observe engineered tissue structure and biochemical composition, simultaneously.

Since water is a very strong absorber of MIR radiation, the penetration depth that MIR-OCT is likely to achieve will obviously be dependent upon the water content. For tissues containing a high concentration of water, such as tendon, the penetration will only be a few hundreds of microns, which is still extremely useful for monitoring the growth of tissue-engineered constructs. However, for tissues with much lower water content, such as bone or the stratum corneum of the skin, we can expect a higher penetration, within the range of 1–2 mm.

II. MID-INFRARED OPTICAL COHERENCE TOMOGRAPHY SYSTEM

A. Broadband quantum cascade laser

The first broadband quantum cascade laser (QCL) to be made for the MIR-OCT system was designed to emit continuously between 6 and 8 μm . The InGaAs/AlInAs QCL contains 11 different active regions of the so-called “three well vertical transition” type,¹⁰ each repeated either three or four times to give 36 active stages in total. The wavelength can be varied by changing the thickness of the active region’s quantum wells and was designed to decrease monotonically across the structure, covering the spectral range from 6 to 8 μm .¹¹

The laser was grown by molecular-beam epitaxy. A 600 nm thick low-doped ($n \approx 3 \times 10^{16} \text{ cm}^{-3}$) InGaAs buffer layer was first grown on low-doped ($n \approx 2 \times 10^{17} \text{ cm}^{-3}$) InP substrate, which simultaneously acts as the bottom cladding. The active waveguide core, consisting of active and bridging regions of the multiwavelength QCL, was capped by 230 nm of low-doped ($n \approx 6 \times 10^{16} \text{ cm}^{-3}$) InGaAs, 2.4 μm of low-doped ($n \approx 1 \times 10^{17} \text{ cm}^{-3}$) InP, and 800 nm of high-doped ($n \approx 7 \times 10^{17} \text{ cm}^{-3}$) InP. The wafer was then processed into mesa etched ridge waveguide lasers of several widths varying between 24 and 56 μm . The ridges were cleaved into 2 mm long bars. The QCL is then mounted onto a TO-5 package.

This emission wavelength range was selected because the absorption of collagen-based tissue constructs is dominated in this region by protein amide I, II, and III bands at approximately 6, 6.5, and 8 μm , respectively. In order to perform differential absorption imaging, another source designed to emit between 8 and 11 μm , where protein absorption is much weaker, is being made. In principle, both lasers could be mounted adjacent to each other and a translation of the cryostat by the distance of their separation (a few hundred microns) could be used to switch between sources. However, in the first instance, the 6–8 μm QCL was considered a good test case to determine the feasibility of performing depth scans where there is significant sample absorption and dispersion. A further complication is water absorption which is also very strong at approximately 6.1 μm due to the bending vibration. Since water will severely limit the penetration depth, initially, collagen samples will be measured following desiccation.

Ideally, the source emission spectrum would be a broad Gaussian shape, producing a narrow Gaussian interference envelope. For a Gaussian, source the coherence length l_c and, therefore, the OCT depth resolution is given by³

$$l_c = \frac{2 \ln 2}{\pi} \frac{\bar{\lambda}^2}{\Delta\lambda},$$

where $\bar{\lambda}$ is the center wavelength and $\Delta\lambda$ is the full width at half maximum. Hence, at the longer wavelengths of the MIR region, the spectral width must increase in a quadratic manner to maintain axial resolution. For example, an ideal broadband MIR source that is centered at 7 μm and has a spectral width of 2 μm would have a coherence length of approximately 11 μm .

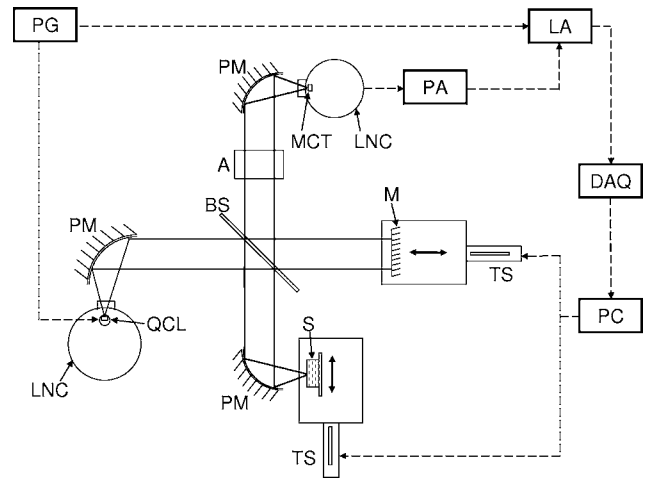


FIG. 1. Schematic of MIR-OCT system. Letter abbreviations in the figure are as follows: A, attenuator; BS, beam splitter; DAQ, data acquisition card; LA, lock-in amplifier; LNC, liquid nitrogen cryostat; M, mirror; MCT, mercury cadmium telluride detector; PA, preamplifier; PC, personal computer; PG, high voltage pulse generator; PM, 90° off-axis paraboloid mirror; QCL, quantum cascade laser; S, sample; and TS, translation stage.

B. Optics and detection

It should be emphasized that the developed features of NIR-OCT cannot simply be transferred for implementation in a MIR-OCT system. Sources, detectors, and other optical components are not transferable, and, also, there is a fundamental difference in the way MIR radiation interacts with tissue. In contrast to NIR wavelengths where scatter limits light penetration in tissue, scatter is less significant at the longer wavelengths of the MIR region. However, light penetration is limited by absorption and, in particular, water absorption.

The current MIR-OCT system is based on a free-space Michelson interferometer and a schematic is shown in Fig. 1. The QCL is mounted within a liquid nitrogen cooled cryostat with a zinc selenide window. The TO-5 package containing the QCL is housed within a custom made copper mount that screws directly into the cold surface of the cryostat. Operating the laser at 77 K enables greater power output and stability. The QCL is driven by a high voltage nanosecond pulse generator, typically at 10 kHz with 300 V square pulses of 150 ns duration. A thin window of germanium with a broadband antireflective coating on one surface is used as a beam splitter. The QCL is polarized perpendicularly to the vertical and the beam splitter plane of incidence, giving a reflectance of 0.48. Axial scans of the reference mirror are performed using a computer-controlled translation stage.

MIR light is focused onto the sample using a 90° off-axis parabolic mirror of focal length of 25.4 mm giving a transverse resolution ($\Delta x = 4\lambda f / \pi D$, where λ = mean wavelength, f = focal length, and D = spot size on focusing mirror = 5 mm) of approximately 45 μm . The corresponding depth of focus (confocal parameter, $b = \pi \Delta x^2 / 2\lambda$) is approximately 460 μm . Focusing optics with a higher numerical aperture could have been used to give better lateral resolution, although that would be at the expense of shorter depth of focus. Thus, a compromise had to be made such that the lateral resolution would remain approximately constant over

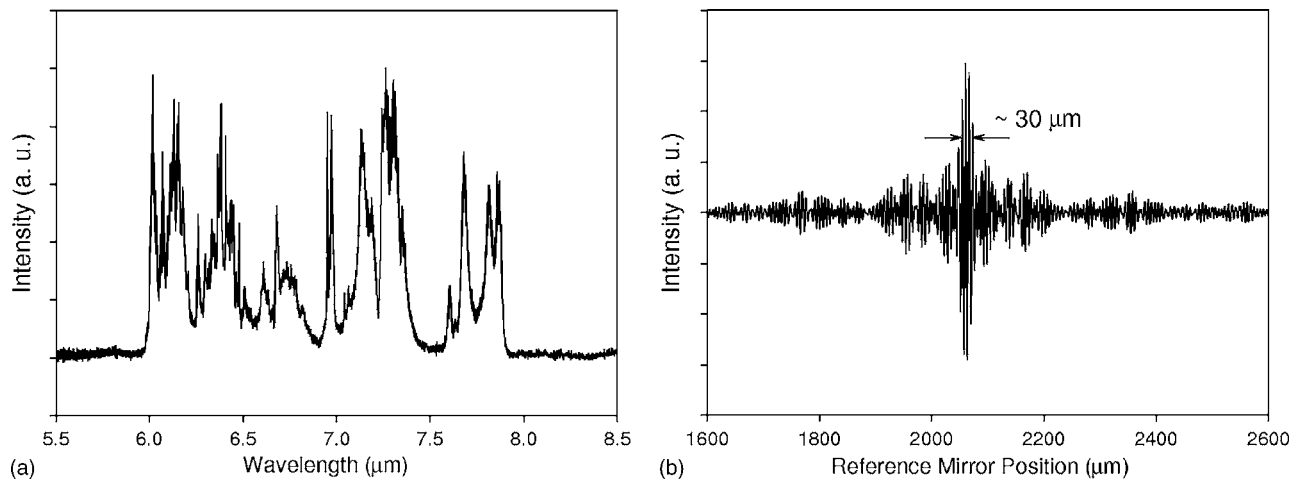


FIG. 2. (a) Low temperature (77 K) high resolution (0.12 cm^{-1}) emission spectrum of the 2 mm long and $36 \mu\text{m}$ wide broadband QC laser ridge operating in pulsed mode (50 ns pulse duration), with repetition rate of 15 kHz and current density of 6.5 kA/cm^2 . (b) Corresponding interferogram.

a large depth. Lateral scans of the sample are also performed using a computer-controlled translation stage.

MIR light is detected using a liquid nitrogen cooled photoconductive mercury cadmium telluride (MCT) detector. An ultralow noise preamplifier is used with a gain of approximately 100 and a -3 dB bandwidth of 2.5 MHz, and the subsequent signal is fed into a lock-in amplifier (10 kHz reference signal). The output is stored on a personal computer (PC) via a 16 bit data acquisition card, and the entire system including reference mirror and sample scanning is controlled using LABVIEW.

Alignment of the system was not a trivial issue and was achieved as follows. A small spot of highly scattering titanium dioxide paint was placed on the copper QCL mount at $<0.5 \text{ mm}$ away from the QCL facet. A red 635 nm diode laser was focused onto the paint spot and the scattered light follows a similar path through the system optics as the divergent output of the QCL. Since the germanium beam splitter does not transmit visible light, a zinc selenide beam splitter was used for initial alignment of the red light. Zinc selenide also works reasonably well as a MIR beam splitter making it possible to determine that the MIR and visible light were following a similar path through both interferometer arms and to the detector. The zinc selenide beam splitter was then replaced with germanium and, by making a few small adjustments to the optics, the signal could be maximized. A better way to do this would have been to use the type of beam splitter employed in Fourier transform infrared (FTIR) spectrometers. These typically have a substrate, such as potassium bromide, which transmits both visible and MIR lights and a thin coating of germanium on one surface with a small hole through which the visible laser light passes. This type of beam splitter will be used in future versions of the system.

III. MEASUREMENTS

A. QCL emission spectrum

Figure 2(a) shows the typical emission spectrum (at 77 K) of the $6\text{--}8 \mu\text{m}$ QCL measured with 0.12 cm^{-1} resolution using a FTIR spectrometer (Bruker IFS 66v/s) in step scan mode. The laser exhibits multiwavelength operation,

and at current densities greater than four times the threshold current, laser action across a continuous band between 6 and $8 \mu\text{m}$ was observed. The peak optical power was 300 mW at 77 K with a repetition rate of 15 kHz, a pulse length of 50 ns, and a current density of 6.5 kA cm^{-2} .

The source interferogram obtained using the Michelson interferometer within the FTIR spectrometer is shown in Fig. 2(b). The position of the scanning mirror was verified by measuring an interferogram for a single mode QCL with distributed feedback emitting at $10.3 \mu\text{m}$. The estimated coherence length of the broadband QCL at current densities of 6.5 kA/cm^2 is about $30 \mu\text{m}$ if only the central peak is considered. However, due to the discrete nature of the emission spectrum, the interferogram exhibits a number of side lobes with significant intensity. The result is a severe degradation of the axial resolution. This is illustrated most clearly in the following experiment.

B. OCT imaging of a calcium fluoride window

As an initial demonstration of the system as a Michelson interferometer, a calcium fluoride (CaF_2) window was used as the target sample, with a thickness of $450 \pm 20 \mu\text{m}$ as measured with digital calipers. CaF_2 has a refractive index of approximately 1.37 at $7 \mu\text{m}$ which is similar to the refractive index of biological tissue. However, in contrast to biological tissues, CaF_2 absorption is negligible at these wavelengths. Figure 3(a) shows the OCT image of the CaF_2 window and is comprised of 80 depth scans with a lateral step size of $20 \mu\text{m}$. The corresponding envelope of a single depth scan, obtained by rectification and smoothing of the interferogram, is shown in Fig. 3(b). The two strongest peaks are separated by $636 \mu\text{m}$ which, when scaled by the refractive index, gives a CaF_2 thickness of $464 \mu\text{m}$. Although the two interfaces can be observed, there are many other peaks of significant intensity. These side lobes can be observed at large distances $>1 \text{ mm}$ away from the actual interfaces. On first inspection, some of these peaks seem indistinguishable from noise. However, their repetition in adjacent scans demonstrate that they are, in fact, side lobes resulting from the somewhat coherent nature of the source.

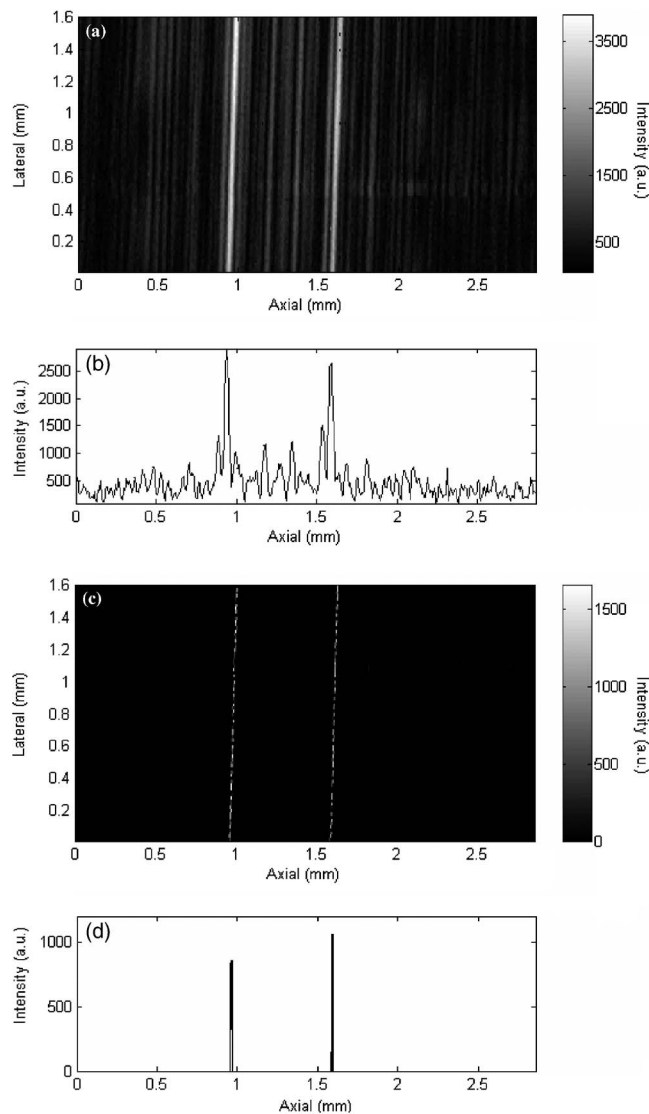


FIG. 3. (a) OCT Image of a CaF_2 window. (b) Interference envelope of one of the constituent depth scans. (c) Deconvolved OCT Image of a CaF_2 window. (d) Deconvolved depth scan.

An important aspect of this research is to develop a satisfactory means of compensating for the mode structure in the QCL output, which produces artifacts in the interferometric signal. Postdetection methods to deconvolve the effects of mode structure from the detected signal can be used.

The axial point spread function (PSF) for the system is easily obtained by recording the interference envelope resulting from a highly reflecting sample (i.e., a mirror). Assuming the PSF is depth invariant, standard analytical or numerical deconvolution methods can be applied to eliminate (or at least substantially reduce) its effect from an OCT scan. For the data in Figs. 3(a) and 3(b), a simple Fourier deconvolution method was sufficient, with Wiener filtering applied to reduce the influence of high frequency noise. The resulting image is shown in Fig. 3(c), which now clearly shows the two reflecting layers of the calcium fluoride window. An example of a single deconvolved depth scan is shown in Fig. 3(d). While this approach will work well for samples consisting of nonabsorbing discrete layers, simple deconvolution methods may be less effective if absorption and dispersion

within the sample results in an axial PSF which changes with depth.

C. Surface topography of a gold/palladium-coated tissue sample

Given the limitations of the initial broadband QCL laser developed for this project, our first measurements on collagen-based tissue constructs were performed in order to map the surface topography of an appropriate sample. This involves detecting the interference between the primary reflection and the reference beam, and, therefore, no deconvolution is required. To verify such measurements, we acquired data on samples which had previously been imaged using scanning electron microscopy (SEM). Preparation for SEM scanning involves coating the sample with a thin layer of a gold-palladium alloy. Thus, this has the very considerable additional advantage that the surface reflectance is high, and the data do not contain reflections from deeper layers.

The samples studied were three-dimensional (3D) collagen lattices embedded with glass rods [mole fractions: 0.5 (P_2O_5), 0.25 (CaO), 0.25 (Na_2O)]. Collagen lattices were polymerized in rectangular molds with glass rods, compressed to form a sheet then rolled along the long axis to form a spiral. Spiral constructs were fixed overnight and then underwent critical point drying and coating with gold-palladium prior to SEM imaging. Figures 4(a) and 4(b) show SEM images of the outer surface of the spiral construct. The embedded glass fibers are not discernible at the surface. However, collagen fiber bundles can be delineated with diameters ranging from 25 to 150 μm . These particular collagen samples embedded with glass fibers are of interest to tissue engineers because the glass is soluble in water. Thus, dissolution of the glass greatly increases the porosity and surface area of the 3D collagen lattices. As far as OCT imaging is concerned, these samples were of interest because, in principle, the 3D distribution of glass fibers within the collagen could be determined.

Figure 4(c) shows a topographical image of the same sample measured using the MIR OCT system. The image was constructed using translation stages to scan a grid of points across the sample with 20 μm between adjacent points in the X and Y directions. At each point, a scan of the reference mirror was performed and the center of gravity of the interference envelope was determined, and assumed to correspond to the Z position of the sample surface. The collagen fiber bundles can be seen with a diameter of approximately 50 μm running in the Y direction as expected from the SEM images.

D. Axial depth scan of uncoated tissue sample

Measurements performed on uncoated samples required long collection times due to a poor signal to noise ratio (SNR). For example, one scan of the reference mirror over 2 mm using a 1 μm step size would typically take 30 min. In an attempt to improve the SNR, a boxcar averager was used instead of a lock-in amplifier. The boxcar averager requires

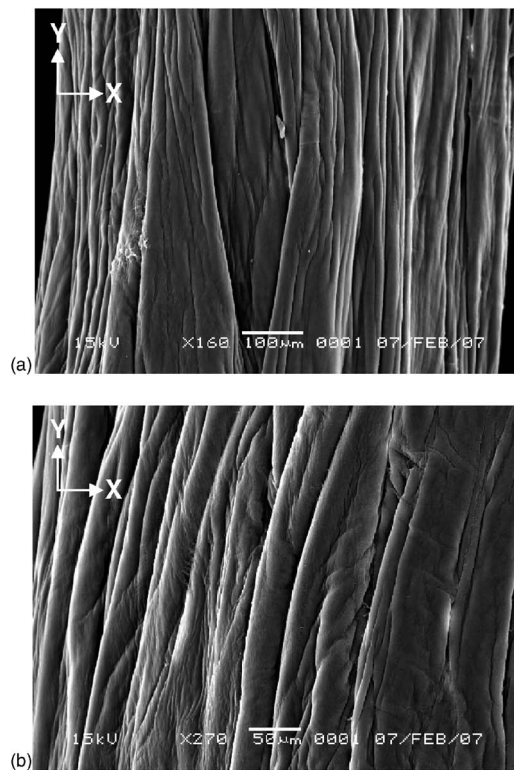
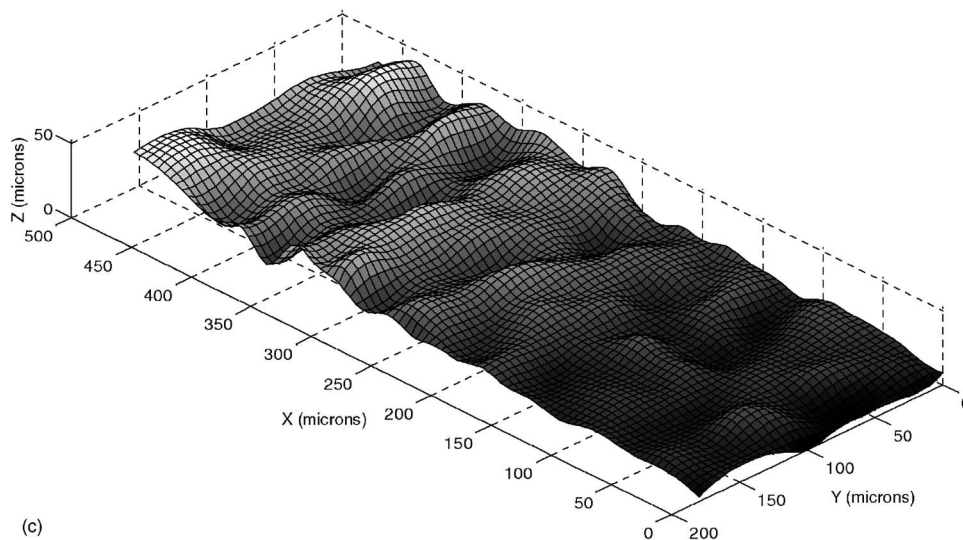


FIG. 4. (a) SEM image of 3D collagen lattice at $\times 160$ magnification. (b) SEM image of 3D collagen lattices at $\times 270$ magnification. (c) Surface topography as measured with mid-infrared OCT system. In (a), (b), and (c) the Y direction corresponds to the long axis of the spiral lattice.



the use of a faster photovoltaic MCT detector. A boxcar window of 250 ns was selected, being slightly longer than the laser pulse length.

Figure 5(a) shows a single axial depth scan of an uncoated 3D collagen lattice containing embedded glass rods. The sample was prepared in a similar method to the gold/palladium-coated sample described above. However, in these samples, the glass fibers are bunched together. The diameter of these bunches are approximately $100\ \mu\text{m}$. In addition, the spiral lattice has been compressed a second time to produce a relatively flat sample with a thickness of approximately $250\ \mu\text{m}$. A simple numerical deconvolution procedure was applied to the data and the result is shown in Fig. 5(b). It is likely that the strongest peak is due to the reflection from the double sided sticky tape on which the sample is mounted, while the smaller peaks to the left probably correspond to

reflective layers within the sample. The peak furthest to the left is believed to be the outer surface of the sample and the other peaks are thought to result from glass bunches and/or the interfaces between each of the $50\text{--}100\ \mu\text{m}$ thick collagen layers of the spiral within the sample. However, given the limitations of the source, the deconvolution method and poor SNR, in addition to a lack of an independent method for comparison, interpretation of these data, at the present stage, is difficult.

IV. DISCUSSION

The measurements reported above demonstrate the first ever results acquired using a mid-infrared OCT system. However, the ultimate aim to acquire depth-resolved OCT images of tissue-engineered samples has so far been frus-

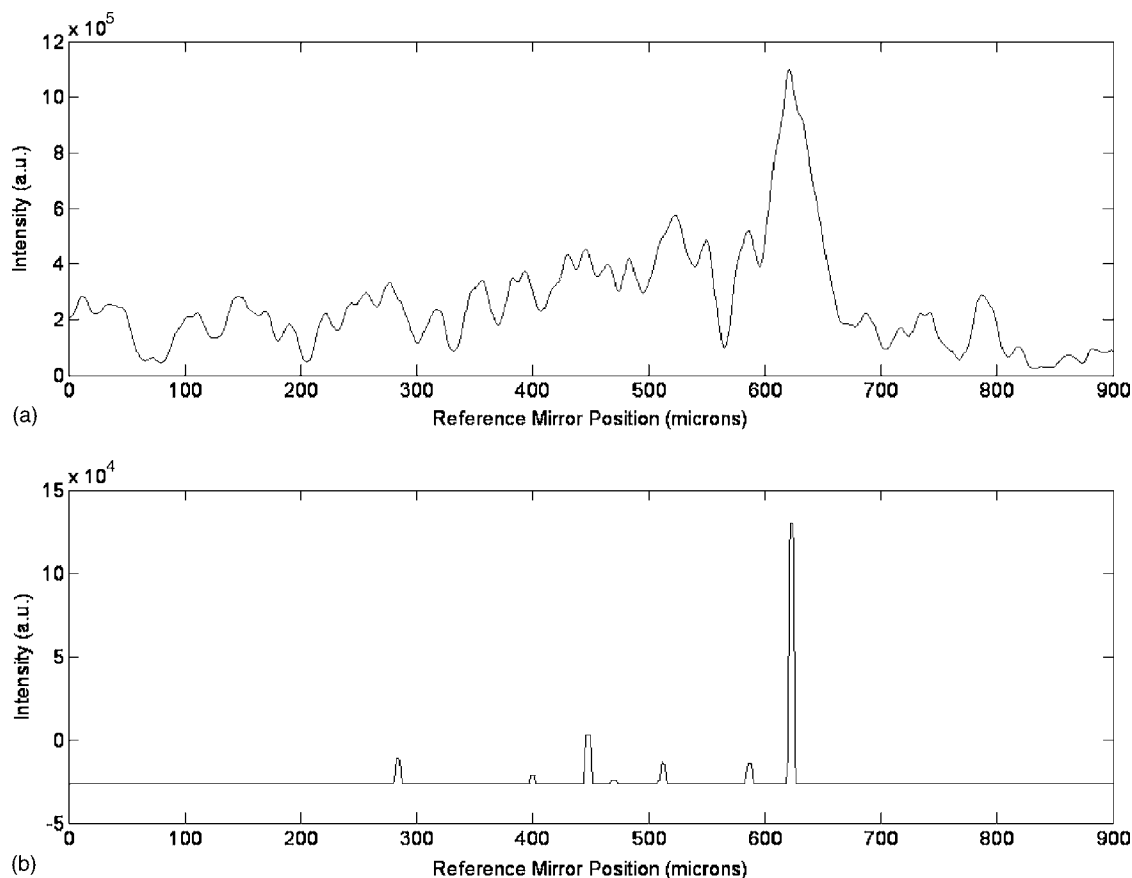


FIG. 5. (a) Interference envelope from axial depth scan of uncoated 3D collagen lattice mounted on double sided sticky tape. (b) Deconvolved axial depth scan.

trated by poor SNR and the difficulties arising from the spectral profile of the QCL source which produces very strong sidebands in the interference signal.

The sensitivity of the current setup needs to be improved. The dynamic range of the system, as defined by the ratio of the maximum to the minimum measurable optical power of the interferometric signal is approximately 30 dB. This is significantly lower than previously reported dynamic ranges for other OCT systems.¹² In other time domain OCT systems, separation of the interference amplitude from the dc component of detected intensity is facilitated by modulation of the optical time delay. Such optical heterodyne detection greatly enhances sensitivity. This is most often achieved by scanning the reference mirror at a constant speed to produce interference modulation at the Doppler frequency or by piezoelectric fiber stretching, although a number of other methods have also been demonstrated. One method that has been explored for the MIR-OCT system is mounting the reference mirror on a piezoelectric stack and oscillating the mirror at approximately 600 Hz. The frequency is limited by the slew rate and maximum current of the driving amplifier, so in principle a much higher frequency could be employed using a faster, more powerful amplifier. However, at the low frequency employed, thus far, this method offers no SNR improvement on the existing setup. This is most likely due to the dominance of $1/f$ noise at low frequency and also to the problem of mechanical vibrations from moving the mirror at high accelerations.

In recent years, there has been a shift away from time domain OCT towards Fourier domain OCT (Ref. 13) which eliminates the need for moving parts to obtain axial scans. As MCT array detector technology continues to develop and becomes more affordable, it is intended that a Fourier domain MIR-OCT will be built.

Work is underway to make the broadband QCL emission more continuous, but there are still some unanswered questions about the factors that determine the degree of continuity in the laser ridge emission. The use of superlattice structures in the QCL is being explored, where lasing occurs between relatively broad minibands, giving rise to a packet of lasing modes over a broad spectral range.¹⁴ However, although this approach should produce a smoother, less discrete emission spectrum, it will not totally resolve the problem with side lobes in the interferogram. A further approach that has been attempted is the development of superluminescence quantum cascade light emitting diodes which emit continuously in the designed region with an emission spectrum that is much closer to an ideal Gaussian.¹¹ However, the problem with such sources at present is insufficient optical power for practical application, although improvement of the power output is currently being investigated.

Another potential technological solution is a supercontinuum source based on photonic crystal fibers, which could offer a much smoother spectral profile. Supercontinuum sources have already been used for OCT in the NIR spectral

region¹⁵ and supercontinuum generation is also possible in the mid-IR spectral region using nonsilica fibers.¹⁶

A major improvement in signal-to-noise ratio could be achieved by converting the existing free-space interferometer to a fiber-based system. Plans are already underway to develop such a system, which would be much more compact and avoid the considerable losses due to the divergence of the MIR beam emitted by the source.

ACKNOWLEDGMENTS

This work has been funded by the EPSRC (Grant No. GR/S77356/01).

¹D. Huang, E. A. Swanson, C. P. Lin, J. S. Schuman, W. G. Stinson, W. Chang, M. R. Hee, T. Flotte, K. Gregory, C. A. Puliafito, and J. G. Fujimoto, *Science* **254**, 1178 (1991).

²J. M. Schmitt, *IEEE J. Sel. Top. Quantum Electron.* **5**, 1205 (1999).

³A. F. Fercher, W. Drexler, C. K. Hitzenberger, and T. Lasser, *Rep. Prog. Phys.* **66**, 239 (2003).

⁴P. H. Tomlins and R. K. Wang, *J. Phys. D* **38**, 2519 (2005).

⁵A. Gh. Podoleanu, *Br. J. Radiol.* **78**, 976 (2005).

⁶J. P. Dunkers, M. T. Cicerone, and N. R. Washburn, *Opt. Express* **11**, 3074 (2003).

⁷Y. Yang, A. Dubois, X.-P. Qin, J. Li, A. El Haj, and R. K. Wang, *Phys. Med. Biol.* **51**, 1649 (2006).

⁸C. Mason, J. F. Markusen, M. A. Town, P. Dunhill, and R. K. Wang, *Phys. Med. Biol.* **49**, 1097 (2004).

⁹C. Mason, J. F. Markusen, M. A. Town, P. Dunhill, and R. K. Wang, *Biosens. Bioelectron.* **20**, 414 (2004).

¹⁰J. Faist, F. Capasso, C. Sirtori, D. L. Sivco, J. N. Baillargeon, A. L. Hutchinson, S. G. Chu, and A. Y. Cho, *Appl. Phys. Lett.* **68**, 3680 (1996).

¹¹E. A. Zibik, W. H. Ng, D. G. Revin, L. R. Wilson, J. W. Cockburn, K. M. Groom, and M. Hopkinson, *Appl. Phys. Lett.* **88**, 121109 (2006).

¹²A. F. Fercher, *J. Biomed. Opt.* **1**, 157 (1996).

¹³A. F. Fercher, C. K. Hitzenberger, G. Kamp, and S. Y. El-Zaiat, *Opt. Commun.* **117**, 43 (1995).

¹⁴J. Faist, M. Beck, T. Aellen, and E. Gini, *Appl. Phys. Lett.* **78**, 147 (2001).

¹⁵G. Humbert, W. J. Wadsworth, S. G. Leon-Saval, J. C. Knight, T. A. Birks, P. St. J. Russell, M. J. Lederer, D. Kopf, K. Weisauer, E. I. Breuer, and D. Stifter, *Opt. Express* **14**, 1596 (2006).

¹⁶J. H. V. Price, T. M. Monro, H. Ebendorff-Heidepriem, F. Poletti, P. Horak, V. Finazzi, J. Y. Y. Leong, P. Petropoulos, J. C. Flanagan, G. Brambilla, X. Feng, and D. J. Richardson, *IEEE J. Sel. Top. Quantum Electron.* **13**, 738 (2007).